The Correlation Between Intergranular Corrosion Resistance and Copper Content in the Precipitate Microstructure in an AA6005A Alloy

Calin D. Marioara[1*], Adrian Lervik[2], Julie Grønvold[3], Otto Lunder[1], Sigurd Wenner[1], Trond Furu[4] and Randi Holmestad[2]

[1]SINTEF Industry, N-7465 Trondheim, Norway

[2] Department of Physics, Norwegian University of Science and Technology (NTNU), N-7491 Trondheim, Norway

[3] Department of Materials Science and Engineering, Norwegian University of Science and Technology (NTNU), N-7491 Trondheim, Norway

[4] Norsk Hydro ASA, N-0283 Oslo, Norway

* Corresponding author. Email: calin.d.marioara@sintef.no

Abstract

A positive correlation is observed between the amount of Cu incorporated in hardening precipitates and intergranular corrosion resistance in an artificially aged Cu-containing 6005A alloy. Three mechanisms have been identified to increase Cu absorption in hardening precipitates: by increasing aging temperature, by pre-deformation and by slow cooling from solution heat treatment. These findings demonstrate the possibility for development of new processing routes to produce Cu-containing Al-Mg-Si alloys with improved corrosion resistance.

Introduction

Al-Mg-Si(-Cu) (6xxx) alloys are widely used in automotive and construction industries due to their high strength, ductility, corrosion resistance and low weight. Usually, such alloys are cast and homogenized, during which dispersoidal AlSiMnFe particles with sizes in the order of ~ 100 nm form in the Al matrix, controlling grain size evolution during a subsequent extrusion step [1,2]. Large (~ μm) primary particles containing the same elements as the dispersoids are also present in the microstructure [3]. As the temperature during extrusion reaches more than 500°C, most of the Mg, Si and Cu elements are in solid solution. However, a further solution heat treatment (SHT) is sometimes performed before the final artificial aging (AA) [4]. Al-Mg-Si(-Cu) alloys are predominantly used in an aged state because they are strengthened by the formation of high numbers of nano-sized metastable precipitates in the Al matrix during the AA. This is a very complex process, and everything that occurs after extrusion or after the SHT influences the numbers, size distribution and types of metastable precipitates [5-9]. Therefore, parameters such as cooling rate from extrusion or SHT, room temperature (RT) storage time and pre-deformation before AA, as well as AA temperature and time are crucial for the material properties. To be able to optimize properties and design new alloys, the processes happening at the micro- and nanoscale must be studied and understood.

Cu additions to Al-Mg-Si alloys in general increases strength and thermal stability [7,10], but often at the expense of a reduced intergranular corrosion (IGC) resistance [11,12]. Hence, this work investigates possible ways of improving IGC resistance of Cu-containing Al-Mg-Si alloys by manipulating the thermo-mechanical processes leading to the condition of the final product. Recent works indicate that IGC propagates due to the presence of a continuous Cu film along the grain boundaries (GBs), and that IGC resistance increases at over-aged conditions due to induced discontinuity in this film [13,14]. On the other hand, Cu additions modify the precipitation sequence by suppressing the β" phase responsible for the peak hardness in Al-Mg-Si alloys and new, Cu-containing phases are created [7]. Therefore, the idea behind the present work is to maximize Cu absorption in the bulk precipitates, thus leaving less Cu available to form a continuous Cu film at the GBs. Ideally this should occur near the peak hardness for a hard and corrosion resistant material to be obtained. To achieve this, the following manipulations of the heat treatment were tried:

a) Change of aging temperature. It is well known that peak hardness is obtained after shorter times at higher temperatures [5,15]. Therefore, for the same aging time, conditions with similar hardness can be obtained, which are underaged (when aged at a lower temperature) and overaged (when aged at a higher temperature). It is interesting to investigate the precipitate microstructure in such conditions, especially with regard to the Cu content in the precipitates.

b) Slower cooling from SHT. This will enhance precipitation of large Al-Mg-Si(-Cu) metastable precipitates on dispersoids, which affects the amount of solute available for precipitation in the bulk [16]. Therefore, it is of interest to compare the precipitation in such a condition with another one that is quenched after SHT, for the same aging temperature and time.

c) Apply deformation before aging. This will promote precipitation on the introduced dislocations and change precipitate parameters as compared to an undeformed condition, for the same aging temperature and time [8].

Experimental

The chemical composition of the 6005A alloy is given in Table 1. The cast billets were homogenized with a heating rate of 87°C/h up to 585°C, where they were held for 2 h and 30 min. The cooling rate from 585°C to 250°C was ~ 400°C/h. The material was then extruded into flat bars with a cross-section of 150 x 3.9 mm^2 and subsequently cooled by water spraying at the die exit. After cooling, the profiles were stretched 0.4-0.5 % and cut into 2 m lengths. Finally, the profiles were stored at RT for 2 h before aging at 185°C for 5 h. These procedures are industrial standard for such alloy types and were conducted at Hydro. The material was received in this state. However, to have more control on the final microstructure we solution heat treated the material and processed it further as described below.

For one processing route, three samples, each with 30 x 25 x 3.9 mm^3 dimension were cut from the as-received profiles. Two of the samples were given a SHT of 6 min at 550°C in a salt bath, water quenched (WQ) and RT stored for 2 h. One sample was aged at 185°C and another one at 210°C in oil baths for various periods. Vickers hardness and electrical conductivity were measured for various times during AA up to 48 h, replacing the samples in the oil baths after each measurement. The third sample was SHT for 6 min at 550°C in a salt bath, air cooled (AC) until 50°C was reached, water quenched and RT stored for 2 h. Then it was aged at 185°C in the same manner as the other sample and its hardness and electrical conductivity were measured. For the hardness, a Matsuzawa DVK-1S unit was used, and the electrical conductivity was measured with a Sigmatest 2.069 unit.

For another processing route, as-received extruded profiles were SHT at 540°C for 30 min in a Nabertherm N15/65HA air circulation furnace, water quenched and then stored in a freezer at about -18°C. The profiles were subsequently pre-deformed by rolling (pre-rolled) to 1%, 5% and 10%, kept for 45 min at RT and then aged at 185°C for 5 h in the same air circulation furnace. A heating rate of 200°C/h was used and the alloy was air cooled after aging. Undeformed samples were included for comparison.

Light microscopy (LM) was used to assess the grain size and degree of recrystallization after SHT. The samples were ground with SiC abrasive paper, polished with diamond paste and then anodized prior to examination under polarised light by use of a Leica MEF4M with Jenoptik Laser Optik System camera. The cross-sections parallel to the extrusion or rolling direction were investigated.

Accelerated IGC tests were conducted on selected conditions according to ISO 11846, method B, which involves immersion of small samples (< 20 cm^2 total area) in an acidified electrolyte containing 30 g/l NaCl and 10 ml/l 35% HCl for 24 h. The ratio of the solution volume to the total sample surface area was kept constant for all tests and was approximately 20 cm^3 / cm^2. After 24 h the samples were rinsed in running water and corrosion products were removed by dipping the samples in concentrated nitric acid for 2 min. The corrosion damage from the IGC tests were studied in bright field LM with the same apparatus as described above. The cross-sections parallel to the extrusion or rolling direction were imaged.

Transmission Electron Microscopy (TEM) was employed to investigate the precipitate microstructure and grain boundaries. For this purpose, samples were cut from the bulk of the materials and electropolished using a Struers TenuPol-5 unit, with a 1/3 nitric acid + 2/3 methanol electrolyte. Three different microscopes were used. First, a JEOL 2100 operated at 200 kV for bright field imaging, equipped with a Gatan Imaging Filter (GIF) for sample thickness determination. Based on the acquired images combined with thickness measurements precipitate statistics were determined, including number densities and volume fractions, based on the methodology described in [5]. Precipitate crystal structures (types) were determined in high-resolution High Angle Annular Dark Field Scanning TEM (HAADF-STEM) mode using an image and probe Cs-corrected JEOL ARM200F operated at 200 kV, with 0.08 nm probe size and 50 mrad inner collector angle. Energy Dispersive X-ray Spectroscopy (EDS) mapping with an Oxford Instrument silicon drift detector and INCA software was performed on a JEOL JEM-2100F operated at 200 kV in analytical STEM mode with 1.5 nm probe size and step size of approximately 3 nm.

The EDS spectrum images (SI) were processed using the open-source python package HyperSpy [17] in the following way: least-square fitting of spectra was performed for every pixel using a 6th order polynomial for the background and Gaussian peaks for each characteristic peak. By inspecting the intensity of different elements, the larger GB particles and dispersoids were masked, enabling line profiles of elemental concentration in the matrix to be created. Smaller, metastable β" particles are also included in the obtained concentration. The intensities obtained from Al, Mg, Si, Cu, Mn and Fe Kα-lines were used for quantification using the Cliff-Lorimer method with theoretically calculated k-factors. The average value along a column at a distance from the GB was estimated for each element along with the standard error of the mean.

Results and Discussion

The LM image of 6005A after SHT presented in Figure 1 shows that the alloy has a fully recrystallized structure. The grains near the surface are larger than the ones in the bulk, which is a consequence of higher temperatures and deformation levels at the surface during the extrusion. However, all TEM investigations are performed in areas from the middle of the profiles, therefore the grain structure is similar in all conditions. The hardness and electrical conductivity evolutions for the samples aged at 185°C and 210°C are shown in Figure 2.

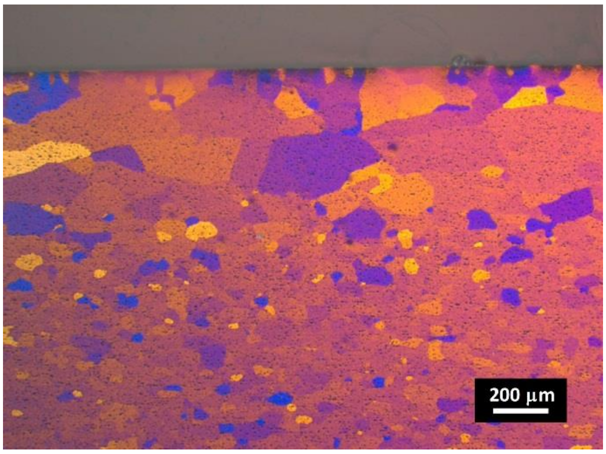

Figure 1 LM of alloy 6005A after SHT, imaging a plane that includes the extrusion direction. The surface grains are much larger than the interior grains.

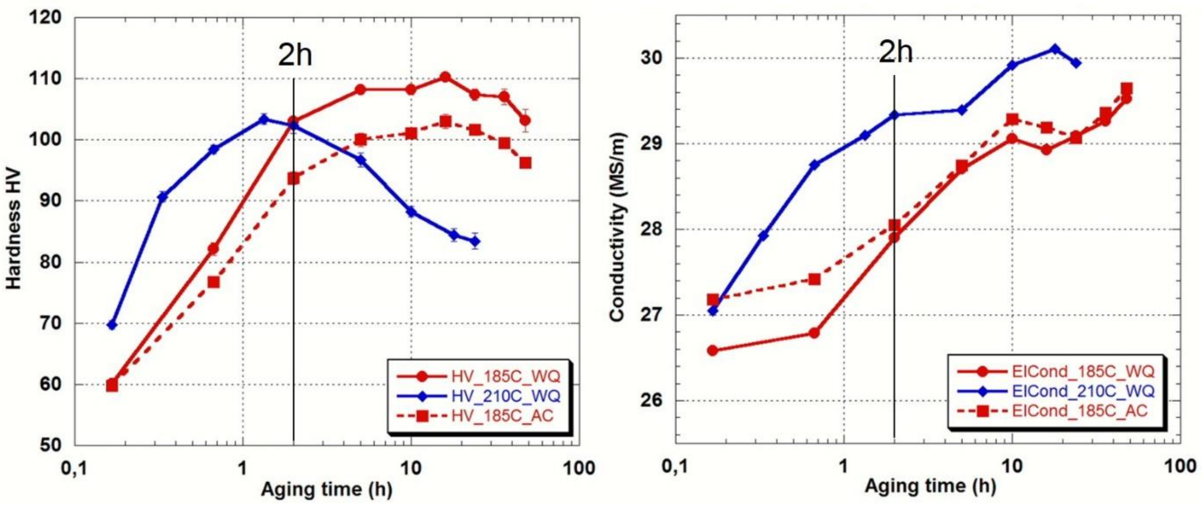

Figure 2 Hardness and electrical conductivity evolution during AA at 185°C with WQ and AC after SHT, and during AA at 210°C with WQ after SHT. As indicated, conditions corresponding to 2 h aging were selected for

IGC testing and TEM investigations. Each value in a given condition is the average of five separate measurements. Standard errors are shown.

Based on these results three conditions were selected for further analysis, labelled as: 185°C_2h_WQ, 210°C_2h_WQ and 185°C_2h_AC. The labelling is indicating the aging temperature, aging time and lastly the cooling method from SHT (WQ or AC). This selection was based on choosing conditions with comparable hardness and not too far from peak hardness, to test their corrosion resistance and correlate it with the precipitate microstructure. As observed, the 185°C_2h_WQ and 185°C_2h_AC conditions are slightly underaged, while 210°C_2h_WQ is slightly overaged. The 185°C_2h_AC is softer, but has similar electrical conductivity to 185°C_2h_WQ. The 185°C_2h_WQ and 210°C_2h_WQ conditions have similar hardness, but different electrical conductivities. For the three conditions, Figure 3 shows average areas of IGC attacks. It is observed that the least resistant condition is 185°C_2h_WQ, while the other two conditions have better IGC resistance. Bright field TEM images from the three conditions are shown in Figure 4, where we observe a dense needle precipitation with needle direction along <100>Al in all conditions. In addition, 185°C_2h_AC has a wider precipitation free zone (PFZ) at GBs, and coarse nucleation of needles on dispersoidal particles. Using the methodology in [5], precipitate parameters were measured and are given in Table 2. For the precipitates nucleated on dispersoids, the number density of dispersoids was measured and it was assumed that on average one precipitate nucleates on one dispersoid.

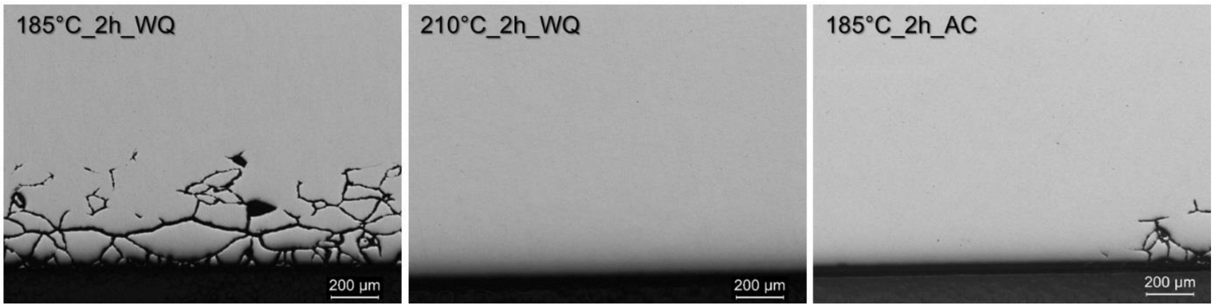

Figure 3 Representative areas of IGC attacks in the three investigated conditions indicated in Figure 2. It can be observed that conditions 210°C_2h_WQ and 185°C_2h_AC have better IGC resistance.

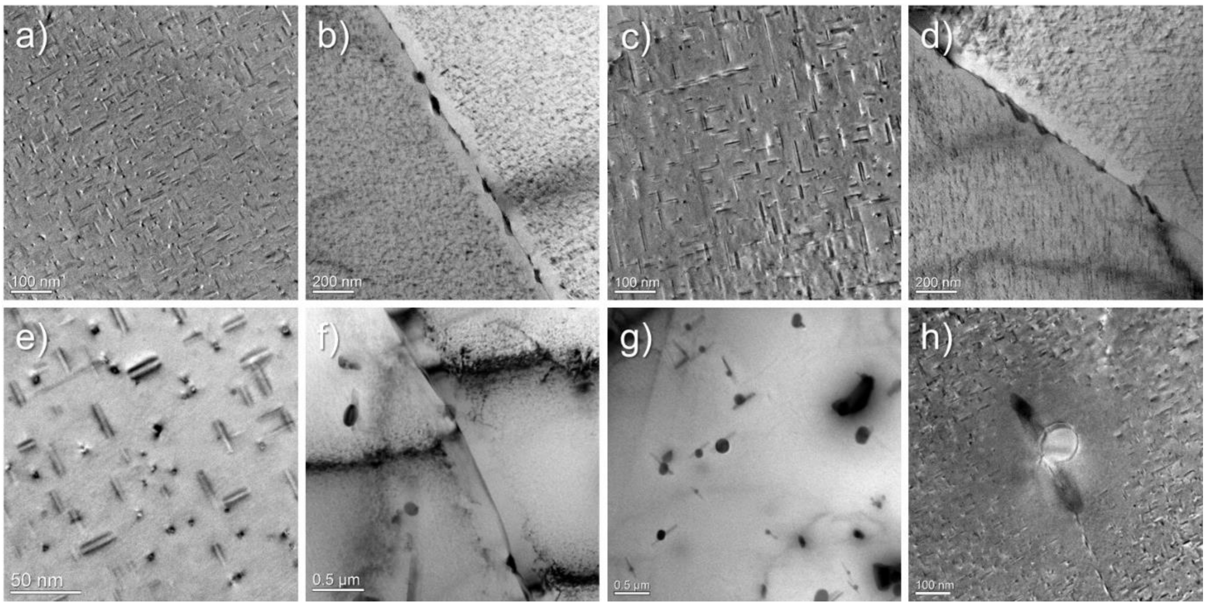

Figure 4 Bright field TEM images from conditions 185°C_2h_WQ (a, b), 210°C_2h_WQ (c, d) and 185°C_2h_AC (e – h). Corresponding precipitate parameters measured from such images are given in Table 2.

Precipitation on dispersoidal particles of coarse needle precipitates is observed in condition 185°C_2h_AC, see g) and h). Images a), c), e) and h) are taken in an <001>Al zone axis.

As stated in the introduction, Cu additions to Al-Mg-Si alloys is detrimental for the IGC resistance. Table 1 shows that alloy 6005A contains 0.14 wt% Cu. It is therefore important to calculate the amount of solute, Cu included, locked into precipitates (the precipitation solute fraction). For this purpose, it is necessary to know both the precipitate volume fraction (from Table 2) and the crystal structure of the precipitates. 50 to 63 high-resolution, Z-contrast HAADF-STEM images of individual precipitates were recorded from each condition at random, and Figure 5 shows representative examples. In principle, the precipitates can be divided into three major types; Type 1 is basically the 'perfect' β" phase with low Cu content. In this case Cu is weakly enriching the Si3/Al sites in both bulk and {320} interface [18,19]. The weak Z-contrast at these sites (but higher than the Si columns contrast) suggests partial column occupancies. Type 2 comprises mixed precipitates (in the same needle as viewed along its length) of β" parts and disordered parts of mainly Cu-containing β'_{Cu} [20] configurations. A lower fraction of Cu-containing Q'/C configurations [20] is also present in some of these precipitates. A third type of precipitates comprises disordered Cu-containing Q'/C with no β" parts. Obviously, Types 2 and 3 are more Cu containing than Type 1, and a simple classification of them for each condition can already give a qualitative indication of the Cu content in the precipitates, see Table 3. It is observed that condition 185°C_2h_WQ contains the highest fraction of the low Cu containing β" phase. Another important observation is that the coarse needles nucleated on dispersoids in condition 185°C_2h_AC have unit cells with spacing that corresponds to the Cu-containing Q' phase, see Figure 6, meaning that an additional amount of Cu is absorbed into them.

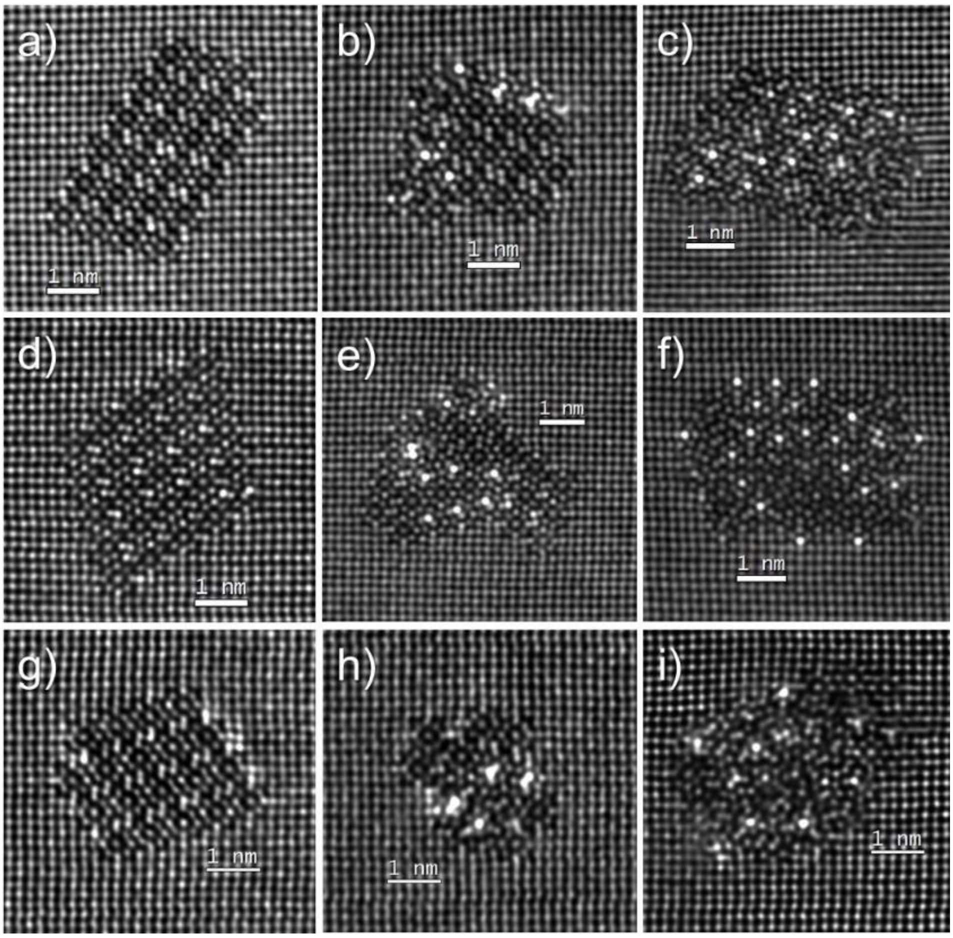

Figure 5 Representative high resolution HAADF-STEM images from conditions 185°C_2h_WQ (a - c), 210°C_2h_WQ (d - f) and 185°C_2h_AC (g - i). Three types of precipitates can be distinguished depending on their crystal structure (viewed here in cross-section): Type 1 (a, d, g) includes 'perfect' β" with low Cu content. Type 2 (b, e, h) is mixed β"/ Cu containing disordered parts and Type 3 (c, f and i) mainly consist of Cu-containing disordered parts. The relative fractions of these types in the three conditions are given in Table 3. The

HAADF-STEM images contain Z-contrast, and the brightest atomic columns contain Cu. The images are recorded in a <001>Al zone axis.

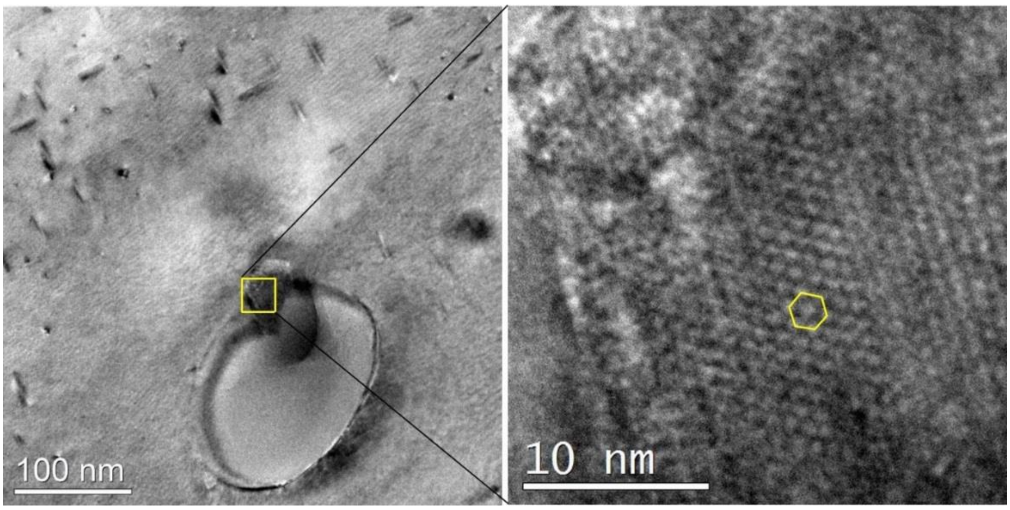

Figure 6 High resolution image (right) of a cross-section belonging to a large particle nucleated on a dispersoid (left) indicates a hexagonal unit cell with 1.04 nm periodicity that is specific for the Cu-containing Q' phase. The images are recorded in a <001>Al zone axis.

The next step was to calculate the solute fraction absorbed into precipitates in each of these three conditions, by combining the precipitate volume fraction with the information about precipitate structure provided by the HAADF-STEM images, and pre-knowledge about unit cell and compositions of individual precipitate-types. The methodology developed for this case is described in the supplementary material. The calculated precipitate solute fractions given in Table 4 indicate that Cu absorption in precipitates is lowest in condition 185°C_2h_WQ at about 0.01 at%, while it is nearly triple for the other two conditions. In this latter case the amount of Cu locked in precipitates is about half of the total Cu amount in the alloy composition. Obviously, more Cu in precipitates implies less Cu elsewhere, including at GBs. It is important to notice that this correlates well with the improved IGC resistance in the 210°C_2h_WQ and 185°C_2h_AC conditions.

An attempt was made to establish a qualitative link between Cu absorption into precipitates and the amount of Cu film observed at GBs. EDS spectrum images (SI) were recorded from the three conditions, and elemental maps for the different elements were created by integrating the characteristic Kα peaks. Maps from one representative SI for each condition are shown in Figure 7. A visual inspection of the Cu map seems to indicate a higher Cu level as a film along the GB in condition 185°C_2h_WQ, in agreement with the concentration line profiles across the GBs shown in Figure 8. We believe the trends observed are correct, but the absolute values represented in these figures are most likely overestimated. The main results can be summarized as follows:

- In all conditions there is a concentration gradient in the PFZ, where Al increases while Mg and Si are depleted when approaching the GB. The Mg/Si ratio in the PFZ is higher than in the bulk-like area. The extension of the concentration gradients correlates with the PFZ widths obtained from STEM images, reported in Table 2.
- In the 185°C_2h_WQ and 210°C_2h_WQ conditions we observe Cu spikes at the grain boundary core, with a larger magnitude in the former. This clear spike is not observed in 185°C_2h_AC. It should be noted that even a discontinuous, or patchy Cu film could still be observed as continuous at the GB, or as a Cu spike in the line profiles, because the GB plane in the 2D TEM image will be projected down to a line. In general, the less Cu is observed in the GB plane, the more probable the Cu film is discontinuous. It is therefore possible that a threshold exists in the Cu concentration, below which the film is discontinuous. More analysis and systematic work is needed to demonstrate it.

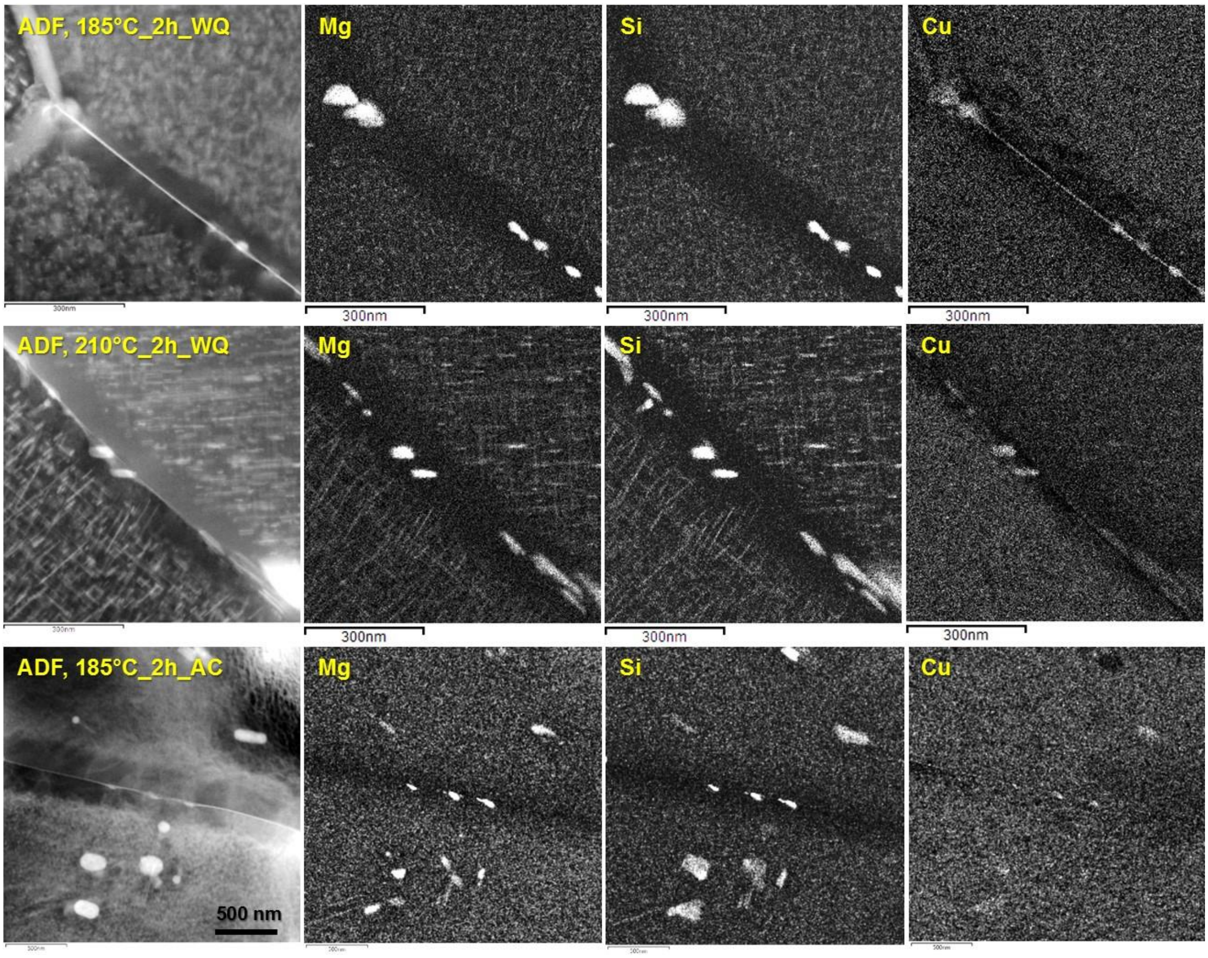

Figure 7 ADF-STEM images and elemental maps from GBs of the investigated conditions. The presence of a continuous Cu film is most pronounced in the condition 185°C_2h_WQ.

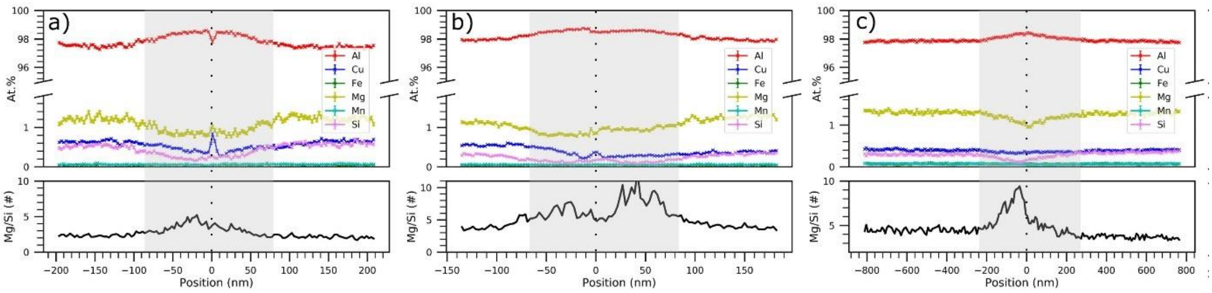

Figure 8 Elemental line profiles (where larger dispersoids and GB precipitates are excluded) along vertical lines parallel to the GB direction for the three maps shown in Figure 7: a) 185°C_2h_WQ, b) 210°C_2h_WQ and c) 185°C_2h_AC. The GB position (middle vertical line) and extent of PFZs are indicated for each profile. It is observed that condition 185°C_2h_WQ has the highest level of elemental enrichment at the GB.

These results point to a correlation between Cu absorption into precipitates, reduced Cu concentrations at GBs and an improved IGC resistance. One way to obtain a higher Cu absorption into precipitates is by increasing aging temperature, which in turn increases the overaging of the peak-hardness β'' phase by formation of mixed β''/Cu-containing precipitates, as well as formation of a higher fraction of Cu-containing phases in general. Another modality for obtaining a higher Cu absorption into precipitates is slower cooling from SHT. This also promotes β'' disorder, and in addition forms large Cu-containing Q' phases nucleated on dispersoids.

The effect of pre-rolling on hardness before and after aging is shown in Figure 9. For the SHT conditions (with no aging) the hardness increases with the deformation level due to work hardening. However, the hardness of the corresponding aged conditions is nearly constant, which indicates that contributions from precipitates decrease with increased deformation levels. This is due to precipitate microstructure coarsening as the result of preferential precipitate formation on introduced dislocations [8].

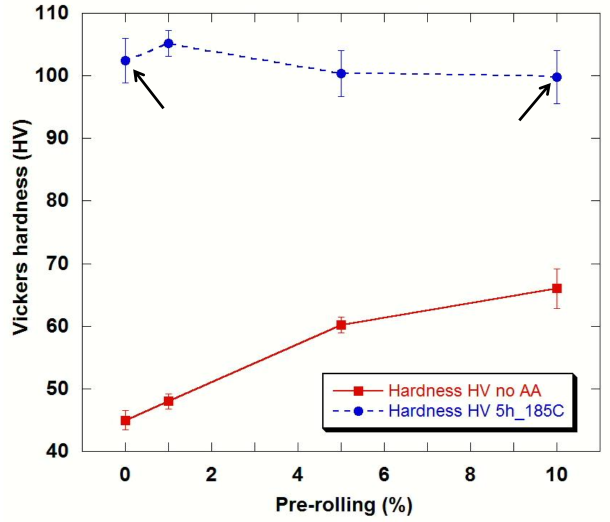

Figure 9 The effect of pre-rolling on hardness. The continuous line connects SHT conditions (no aging) for the different deformation levels. The dashed line connects conditions that were SHT and pre-rolled to different levels, followed by aging for 5 hours at 185°C. These last conditions were IGC tested. The conditions indicated by arrows were selected for TEM investigations.

IGC tests were performed on aged samples with different pre-rolling levels, including the undeformed condition. Images with IGC attacks from representative areas are given in Figure 10. It is interesting to notice that the IGC resistance is improved for the pre-rolling levels of 5% and 10%. TEM bright field images were recorded from the undeformed and 10% pre-rolled conditions (see Figure 11 a) and e)), showing only a homogeneous precipitate distribution in the undeformed case, whilst nucleation of precipitates on introduced dislocation lines is observed in the 10% pre-rolled case, as expected. High resolution HAADF-STEM images show that in the undeformed condition most precipitates are of Type 1 or 2, therefore most of them contain the low Cu content β'' phase. However, in the 10% pre-rolled condition most precipitates, both in the bulk and nucleated on dislocation lines were of Type 3 (non-β''). One difference was that in the bulk the precipitates were smaller and more disordered, while the ones nucleated on dislocation lines were coarser and consisted of more ordered Q' phase. Representative HAADF-STEM images from both conditions are shown in Figure 11 b), c), d) and f). It is clear from these observations that more Cu is incorporated in the precipitates in the pre-rolled condition. EDS elemental maps and line profiles of GBs were made for this condition and a representative example is shown in Figure 12. A small Cu spike at the GB core, with magnitude somewhat similar to that of 210°C_2h_WQ, is observed. Furthermore, the Mg/Si ratio remains constant across the bulk/ PFZ interface for every GB analyzed. This is different from the undeformed conditions, where the ratio was higher in the PFZ. We believe the reason for the higher Mg/Si ratio in the PFZ in the undeformed conditions is due to higher diffusivity of Si towards the GB, as compared to Mg. However, due to the introduction of dislocations in the pre-rolled conditions, the same mechanism would make Si diffuse faster also to the dislocations in the bulk. In this way we would have a similar Mg/Si ratio in both bulk and at the PFZ.

Although precipitate statistics have not been made for these conditions, previous work has shown that higher precipitate volume fractions are obtained if pre-deformation is applied before aging [8]. This information combined with improved IGC resistance in the pre-rolled condition strengthens the hypothesis about a positive correlation between pre-deformation and an increased amount of Cu locked in precipitates.

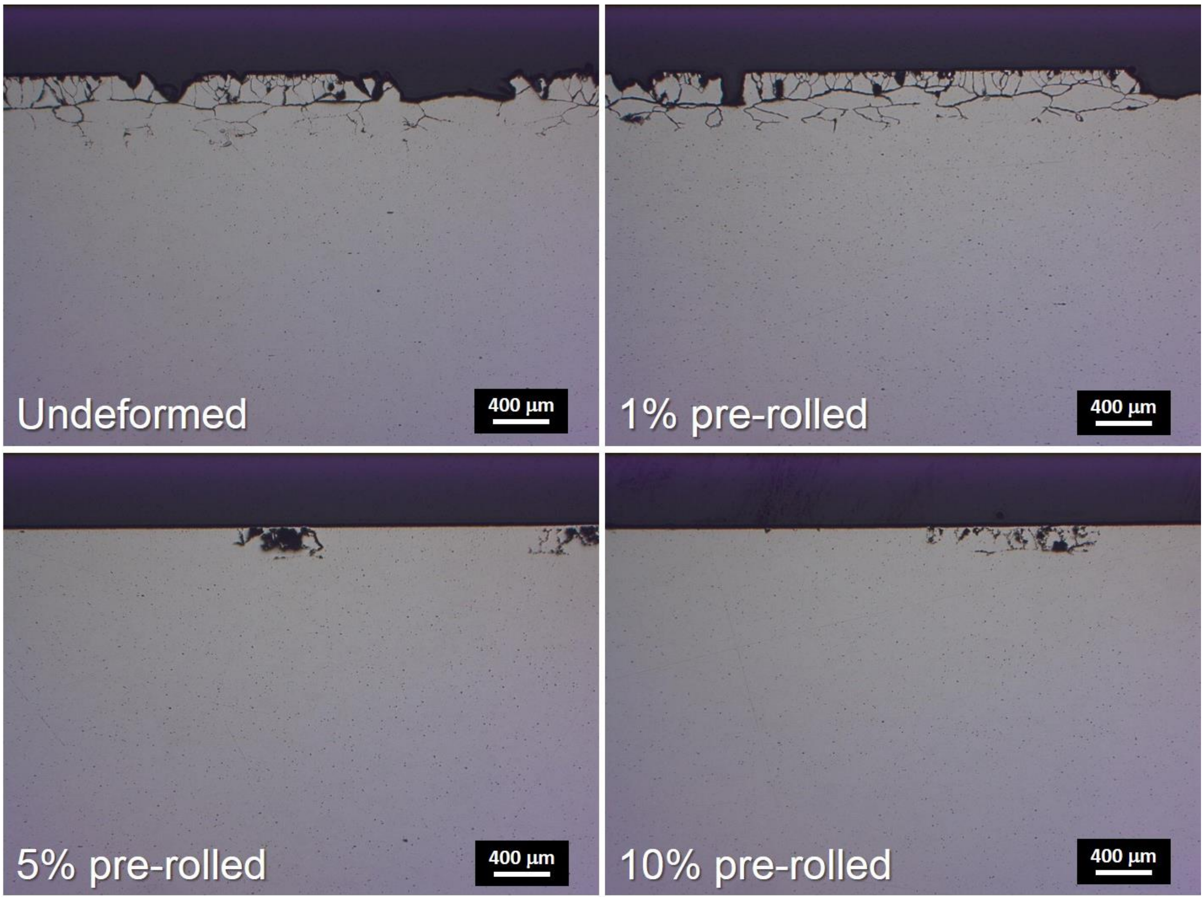

Figure 10 Results of IGC tests in representative areas of alloy 6005A which was SHT, pre-rolled to different levels and artificially aged for 5 hours at 185°C. It is clearly observed that IGC resistance is increasing at high deformation levels.

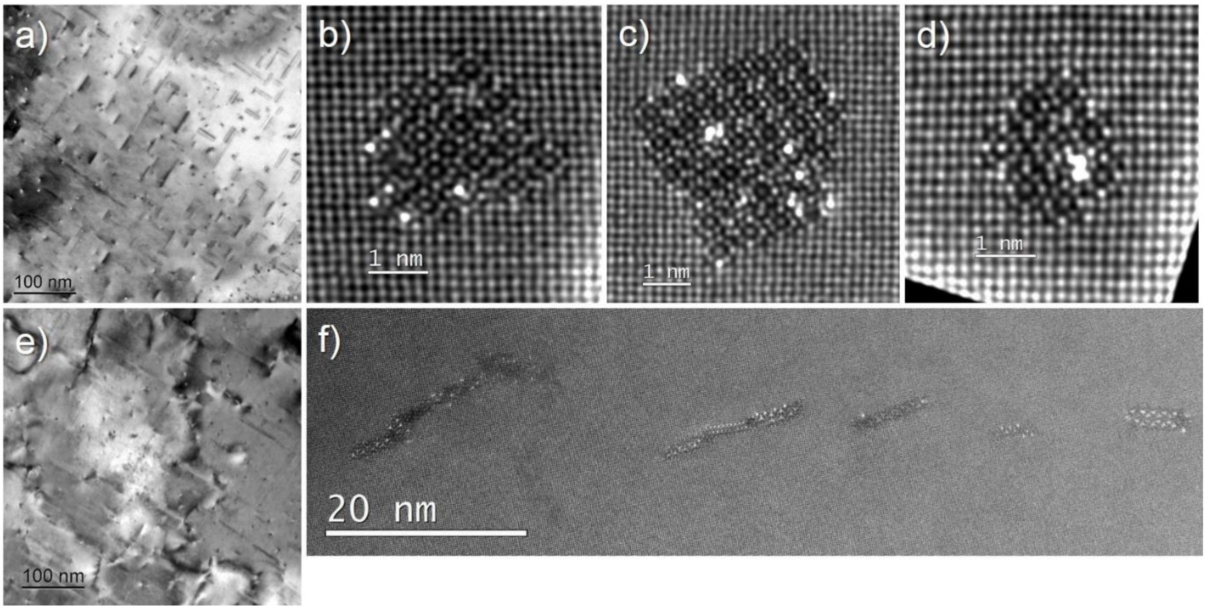

Figure 11 a) Bright field TEM overview image and b) – d) HAADF-STEM images of individual precipitates in the undeformed condition of alloy 6005.40 aged for 5 hours at 185°C. e) Bright field TEM overview image and f) HAADF-STEM image of precipitates nucleated along a dislocation line in the 10% pre-rolled and aged for 5 hours at 185°C condition. A homogeneous, slightly Cu enriched β" precipitate distribution is observed in the undeformed condition, while precipitation of Cu containing precipitates is observed nucleated on dislocation lines in the pre-rolled condition. All images are taken in an <001>Al zone axis.

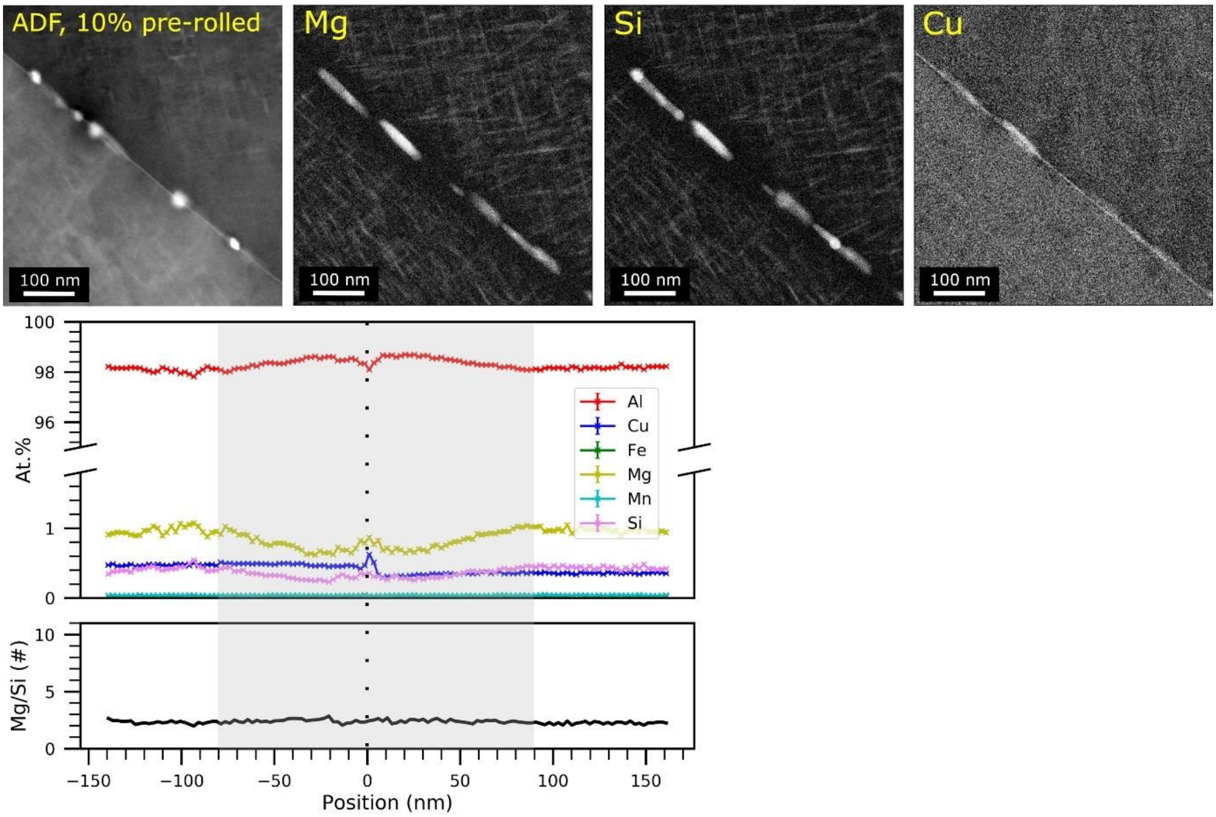

Figure 12 EDX elemental maps and corresponding profiles of the elemental compositions in the matrix (where large dispersoids and GB precipitates are excluded) along vertical lines parallel to the GB direction in the 10% pre-rolled condition. Cu segregation is observed at the grain boundary core and the Mg/Si ratio is nearly constant over the PFZ.

Conclusions

This work demonstrates the possibility of controlling IGC resistance of Cu-containing Al-Mg-Si alloys by manipulation of their thermo-mechanical processing. The key factor is to produce precipitates with high Cu content, by decreasing the fraction of β'' precipitating in the bulk and increasing the fraction of Cu-containing precipitates such as β'_{Cu} and Q'. For practical applications, this should be done without compromising on material strength. Such conditions will have a Cu depleted matrix, resulting in a reduced Cu amount at GBs and reduced susceptibility to IGC. In this context, three possible approaches have been identified:

(1) Increase AA temperature. β'' is the main hardening phase in the Al-Mg-Si alloys, including those with low Cu content. As β'' phase has a low Cu absorption potential, one way to increase Cu content in precipitates is to over-age, but usually this leads to strength loss. An increase in temperature will produce the peak hardness after shorter times, and it might be possible to find a compromise between maintaining hardness and modification of β'' phase (having more Cu content as in Type 2) in a mild over-aging.

(2) A slower cooling from SHT will promote the nucleation of Cu containing Q' phase on dispersoidal particles and will in addition increase disorder in bulk β'' precipitates. However, because a certain amount of Mg and Si solute will also be absorbed in to the large Q' particles, usually these conditions have lower hardness as compared to their water quenched counterparts. In addition, a wider PFZ forming in the slow-cooled conditions may affect material's ductility.

(3) Pre-deformation introduces dislocations which become preferred nucleation sites for Cu-containing precipitates, especially Q'. Increased disorder of bulk precipitates and lower fractions of β'' have also been observed in these conditions.

The above findings can be used as a tool to tailor and improve IGC resistance of Cu containing Al-Mg-Si alloys used in specific applications.

Acknowledgements

This work was supported by the KBP project *FICAL (247598)*, co-financed by The Research Council of Norway (RCN), and the industrial partners Norsk Hydro, Sapa, Gränges, Benteler, and Steertec. The (S)TEM work was carried out on the *NORTEM (197405)* infrastructure at the TEM Gemini Centre, Trondheim, Norway.

References

1. F. J. Humphreys, M. Hatherly, *Recrystallization and Related Annealing Phenomena*, 2nd ed., Elsevier, Oxford, 2004, pp. 469-476.
2. L. Lodgaard, N. Ryum, *Mater. Sci. Eng. A*, 2000, vol. 283, pp. 144-152.
3. S. Zajac, B. Hutchinson, A. Johansson, L.-O. Gullman, *Mater. Sci. Technol*., 1994, vol. 10, pp. 323-333.
4. *Aluminum standards and data, 1978 Metric SI*, 1st ed., the Aluminum Association, Inc., 818 Connecticut Ave. N.W., Washington, D.C. 20006, pp. 53-54.
5. C. D. Marioara, S. J. Andersen, H. W. Zandbergen and R. Holmestad, *Metall. Mater. Trans. A*, 2005, vol. 36A, pp. 691-02.
6. C. D. Marioara, H. Nordmark, S. J. Andersen and R. Holmestad, *J. Mater. Sci*., 2006, vol. 41, pp. 471-78.
7. C. D. Marioara, S. J. Andersen, T. N. Stene, H. Hasting, J. Walmsley, A. T. J. Van Helvoort and R. Holmestad, *Philos. Mag.*, 2007, vol. 87, pp. 3385-413.
8. K. Teichmann, C. D. Marioara, S. J. Andersen and K. Marthinsen, *Metall. Mater. Trans. A*, 2012, vol. 43A, pp. 4006-014.
9. T. Saito, C. D. Marioara, J. Røyset, K. Marthinsen and R. Holmestad, *Mater. Sci. Eng. A*, 2014, vol. 609, pp. 72-79.
10. C. D. Marioara, S. J. Andersen, J. Røyset, O. Reisø, S. Gulbrandsen-Dahl, T. E. Nicolaisen, I. E. Opheim, J. F. Helgaker and R. Holmestad, *Metall. Mater. Trans. A*, 2014, vol. 45A, pp. 2938-2949.

11. G. Svenningsen, M. H. Larsen, J. C. Walmsley, J. H. Nordlien and K. Nisancioglu, *Corrosion Science*, 2006, vol. 48, pp. 1528-43.
12. G. Svenningsen, M. H. Larsen, J. H. Nordlien and K. Nisancioglu, *Corrosion Science*, 2006, vol. 48 pp. 3969-87.
13. M. H. Larsen, J. C. Walmsley, O. Lunder, R. H. Mathiesen and K. Nisancioglu, *Journal of The Electrochemical Society*, 2008, vol. 155 (11), pp. C550-56.
14. S. K. Kairy, P. A. Rometsch, C. H. J. Davies and N. Birbilis, *Corrosion*, 2017, vol. 73, pp. 1280-95.
15. C. D. Marioara, S. J. Andersen, J. Jansen and H. W. Zandbergen, *Acta Mater*., 2003, vol. 51, pp. 789-796.
16. K. Strobel, M. A. Easton, L. Sweet, M. J. Couper, J.-F. Nie, *Mater. Trans*., 2011, vol. 52, pp. 914-919.
17. Francisco de la Peña et al., HyperSpy 1.3. (May 27, 2017), doi:10.5281/zenodo.583693, https://zenodo.org/record/583693#.Wpf1FfmnFaQ. Accessed 1 Mar 2018.
18. K. Li, A. Beche, M. Song, G. Sha, X. Lu, K. Zhang, Y. Du, S. P. Ringer, D. Schryvers, *Scripta Mater*., 2014, vol. 75, pp. 86-89.
19. T. Saito, F. J. H. Ehlers, W. Lefebvre, D. H. Maldonado, R. Bjørge, C. D. Marioara, S. J. Andersen, E. A. Mørtsell and R. Holmestad, *Scripta Mater*., 2016, vol. 110, pp. 6-9.
20. T. Saito, C. D. Marioara, S. J. Andersen, W. Lefebvre and R. Holmestad, *Philos. Mag.*, 2014, vol. 94, pp. 520-31.

Tables

Table 1 Composition of the investigated alloy as measured by Optical Emission Spectrometry.

Alloy/ Element	**Mg**	**Si**	**Cu**	**Mn**	**Fe**
6005A, wt%	0.57	0.64	0.14	0.16	0.21
6005A, at%	0.63	0.62	0.06	0.08	0.10

Table 2 Precipitate needle statistics in the analyzed conditions. All parameters are from the bulk precipitates, with the exception of condition (185°C_2h_AC)* where only the parameters of the precipitates nucleated on dispersoids are given.

Condition/ Parameter	**<Density> (μm^{-3})**	**<Length> (nm)**	**<Cross Section> (nm^2)**	**<Volume Fraction> = D x L x CS**	**PFZ at GBs (nm)**
185°C_2h_WQ	23494 ± 2547	30.58 ± 1.05	8.11 ± 0.22	0.582 ± 0.077	115 to 130
210°C_2h_WQ	17462 ± 2374	38.72 ± 3.15	10.13 ± 0.29	0.685 ± 0.154	125 to 140
185°C_2h_AC	39483 ± 4434	22.89 ± 1.11	7.23 ± 0.19	0.653 ± 0.100	~ 400
(185°C_2h_AC)*	1.16 ± 0.12	478.18 ± 14.51	1537.2 ± 93.28	0.086 ± 0.010	

Table 3 Classification of bulk precipitate types based on the high resolution HAADF-STEM images.

Condition	**Type 1 (%)**	**Type 2 (%)**	**Type 3 (%)**
185°C_2h_WQ	63	22	15
210°C_2h_WQ	21	41	38
185°C_2h_AC	20	60	20

Table 4 Total solute bound in precipitates (precipitate solute fractions) calculated as described in the supplementary material (at%).

Element/ Condition	**Mg**	**Si**	**Cu**	**Al**
185°C_2h_WQ	0.18	0.18	0.01	0.07
210°C_2h_WQ	0.18	0.17	0.03	0.11
185°C_2h_AC	0.20	0.20	0.03	0.11

Figure captions

Figure 1 LM of alloy 6005A after SHT, imaging a plane that includes the extrusion direction. The surface grains are much larger than the interior grains.

Figure 2 Hardness and electrical conductivity evolution during AA at 185°C with WQ and AC after SHT, and during AA at 210°C with WQ after SHT. As indicated, conditions corresponding to 2 h aging were selected for IGC testing and TEM investigations. Each value in a given condition is the average of five separate measurements. Standard errors are shown.

Figure 3 Representative areas of IGC attacks in the three investigated conditions indicated in Figure 2. It can be observed that conditions 210°C_2h_WQ and 185°C_2h_AC have better IGC resistance.

Figure 4 Bright field TEM images from conditions 185°C_2h_WQ (a, b), 210°C_2h_WQ (c, d) and 185°C_2h_AC (e – h). Corresponding precipitate parameters measured from such images are given in Table 2. Precipitation on dispersoidal particles of coarse needle precipitates is observed in condition 185°C_2h_AC, see g) and h). Images a), c), e) and h) are taken in an <001>Al zone axis.

Figure 5 Representative high resolution HAADF-STEM images from conditions 185°C_2h_WQ (a - c), 210°C_2h_WQ (d - f) and 185°C_2h_AC (g - i). Three types of precipitates can be distinguished depending on their crystal structure (viewed here in cross-section): Type 1 (a, d, g) includes 'perfect' β" with low Cu content. Type 2 (b, e, h) is mixed β"/ Cu containing disordered parts and Type 3 (c, f and i) mainly consist of Cu-containing disordered parts. The relative fractions of these types in the three conditions are given in Table 3. The HAADF-STEM images contain Z-contrast, and the brightest atomic columns contain Cu. The images are recorded in a <001>Al zone axis.

Figure 6 High resolution image (right) of a cross-section belonging to a large particle nucleated on a dispersoid (left) indicates a hexagonal unit cell with 1.04 nm periodicity that is specific for the Cu-containing Q' phase. The images are recorded in a <001>Al zone axis.

Figure 7 ADF-STEM images and elemental maps from GBs of the investigated conditions. The presence of a continuous Cu film is most pronounced in the condition 185°C_2h_WQ.

Figure 8 Elemental line profiles (where larger dispersoids and GB precipitates are excluded) along vertical lines parallel to the GB direction for the three maps shown in Figure 7: a) 185°C_2h_WQ, b) 210°C_2h_WQ and c) 185°C_2h_AC. The GB position (middle vertical line) and extent of PFZs are indicated for each profile. It is observed that condition 185°C_2h_WQ has the highest level of elemental enrichment at the GB.

Figure 9 The effect of pre-rolling on hardness. The continuous line connects SHT conditions (no aging) for the different deformation levels. The dashed line connects conditions that were SHT and pre-rolled to different levels, followed by aging for 5 hours at 185°C. These last conditions were IGC tested. The conditions indicated by arrows were selected for TEM investigations.

Figure 10 Results of IGC tests in representative areas of alloy 6005A which was SHT, pre-rolled to different levels and artificially aged for 5 hours at 185°C. It is clearly observed that IGC resistance is increasing at high deformation levels.

Figure 11 a) Bright field TEM overview image and b) – d) HAADF-STEM images of individual precipitates in the undeformed condition of alloy 6005.40 aged for 5 hours at 185°C. e) Bright field TEM overview image and f) HAADF-STEM image of precipitates nucleated along a dislocation line in the 10% pre-rolled and aged for 5 hours at 185°C condition. A homogeneous, slightly Cu enriched β" precipitate distribution is observed in the undeformed condition, while precipitation of Cu containing precipitates is observed nucleated on dislocation lines in the pre-rolled condition. All images are taken in an <001>Al zone axis.

Figure 12 EDX elemental maps and corresponding profiles of the elemental compositions in the matrix (where large dispersoids and GB precipitates are excluded) along vertical lines parallel to the GB direction in the 10% pre-rolled condition. Cu segregation is observed at the grain boundary core and the Mg/Si ratio is nearly constant over the PFZ.

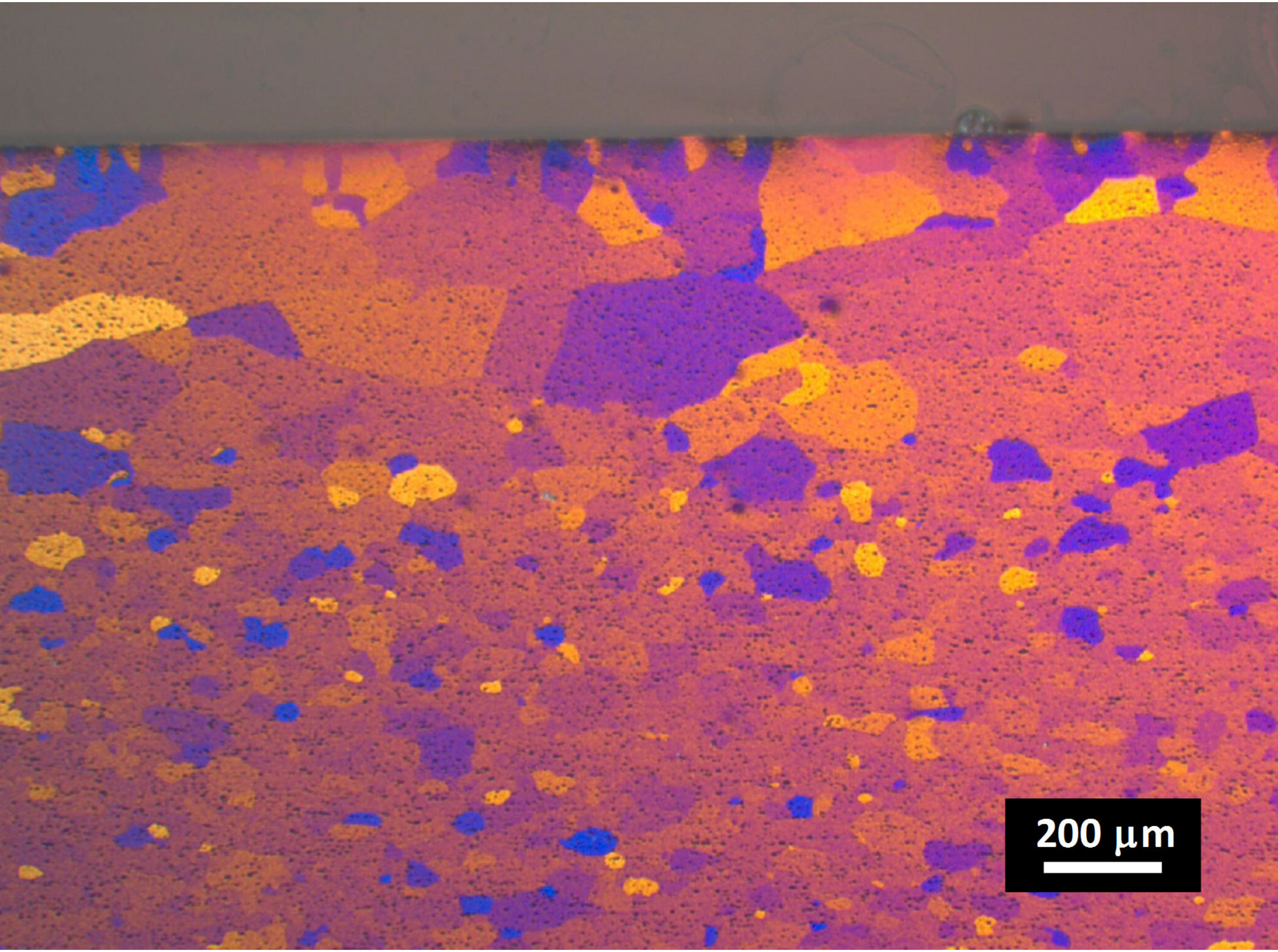
200 µm

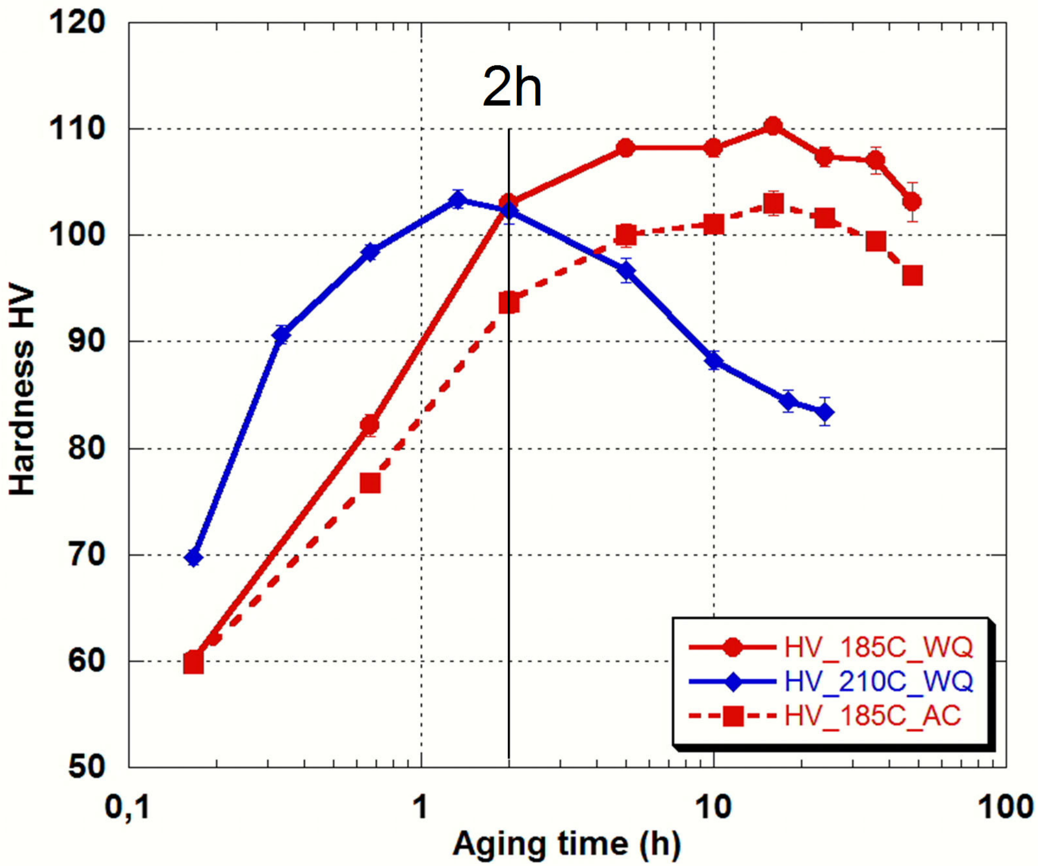
120
110
100
90
80
70
60
50
Hardness HV
2h
HV_185C_WQ
HV_210C_WQ
HV_185C_AC
0,1
1
10
100
Aging time (h)

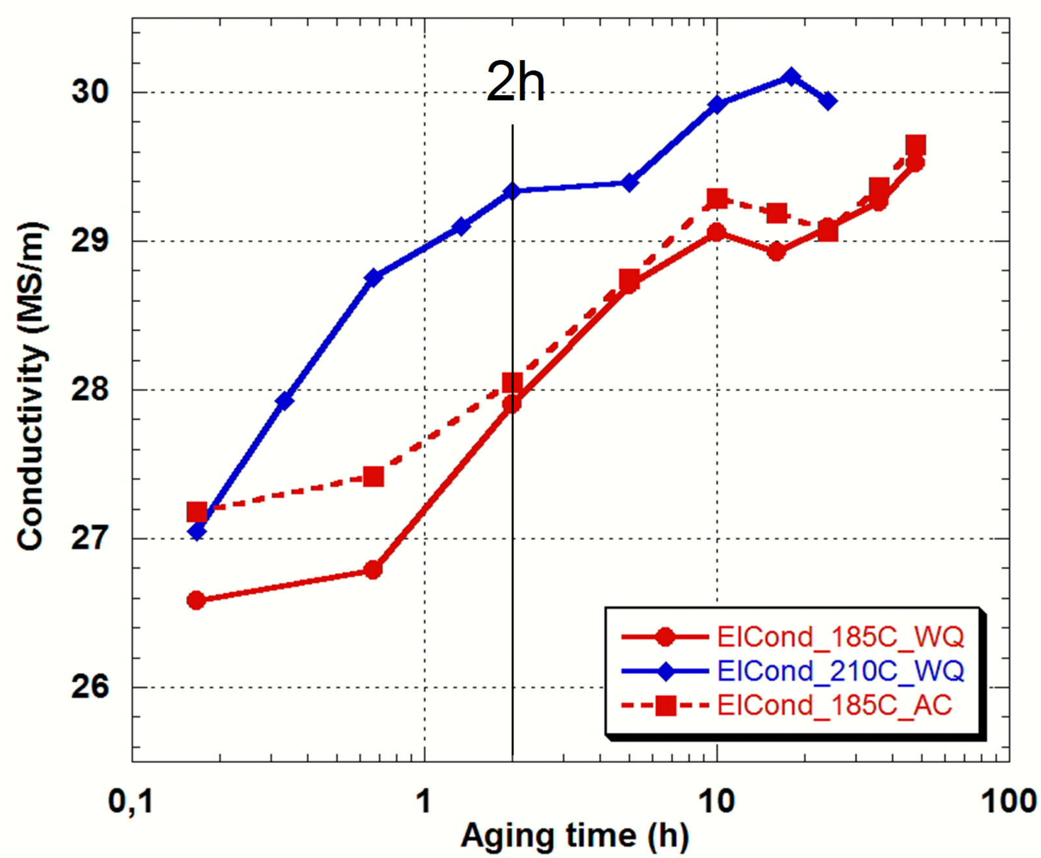
30
29
28
27
26
Conductivity (MS/m)
2h
ElCond_185C_WQ
ElCond_210C_WQ
ElCond_185C_AC
0,1
1
10
100
Aging time (h)

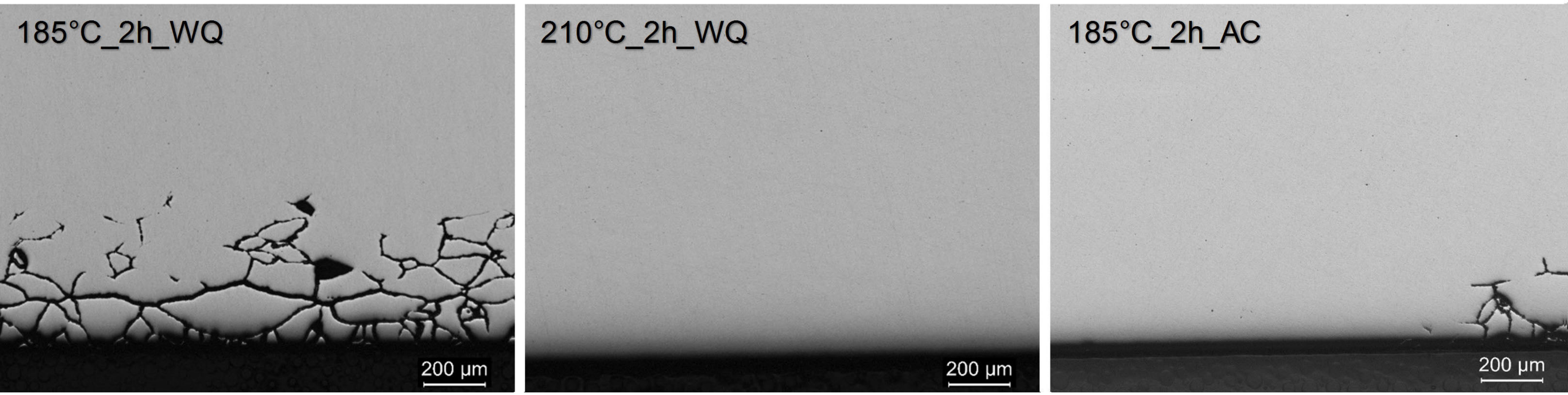
185°C_2h_WQ
200 µm
210°C_2h_WQ
200 µm
185°C_2h_AC
200 µm

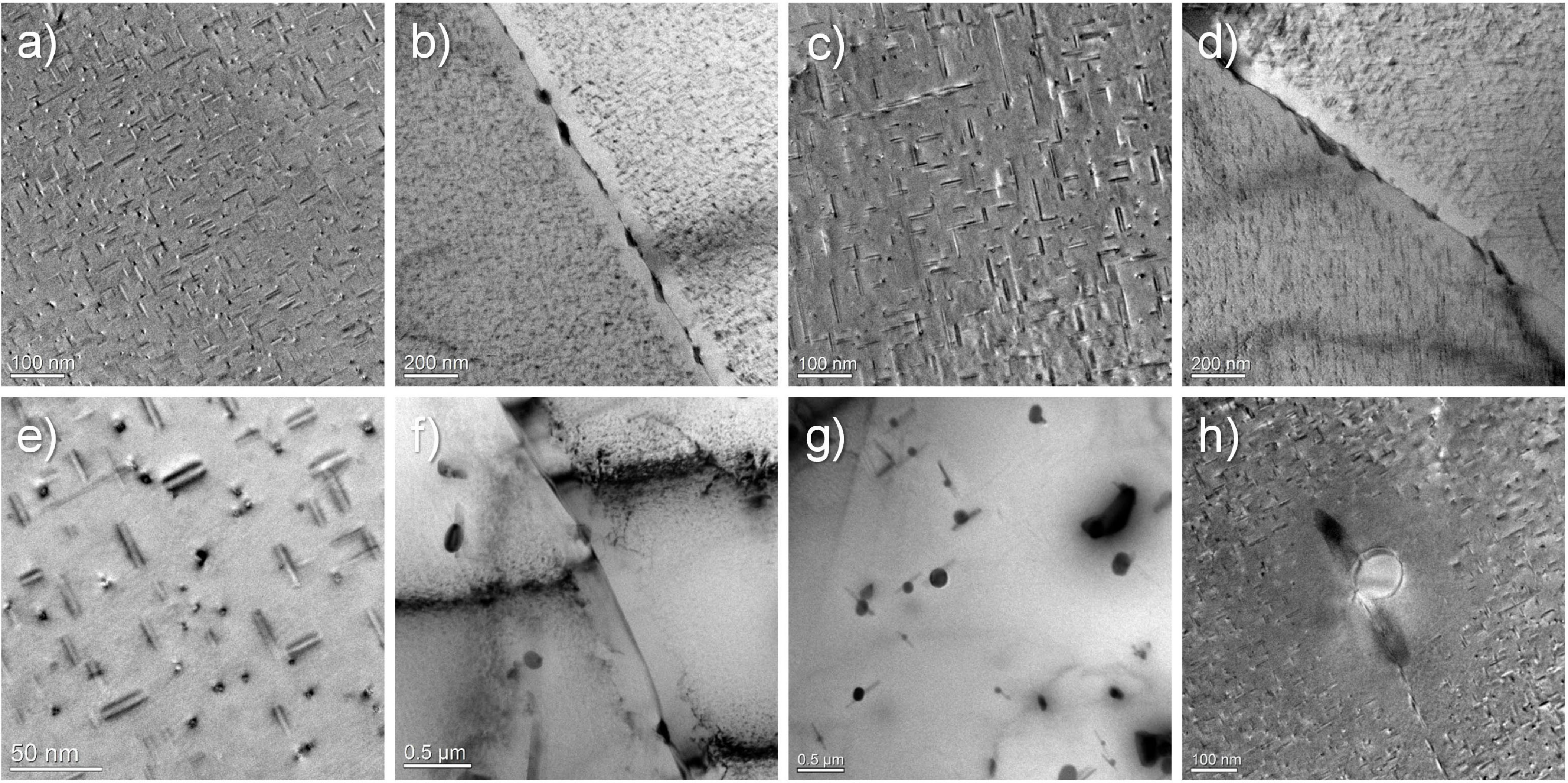
a)
100 nm
b)
200 nm
c)
100 nm
d)
200 nm
e)
50 nm
f)
0.5 μm
g)
0.5 μm
h)
100 nm

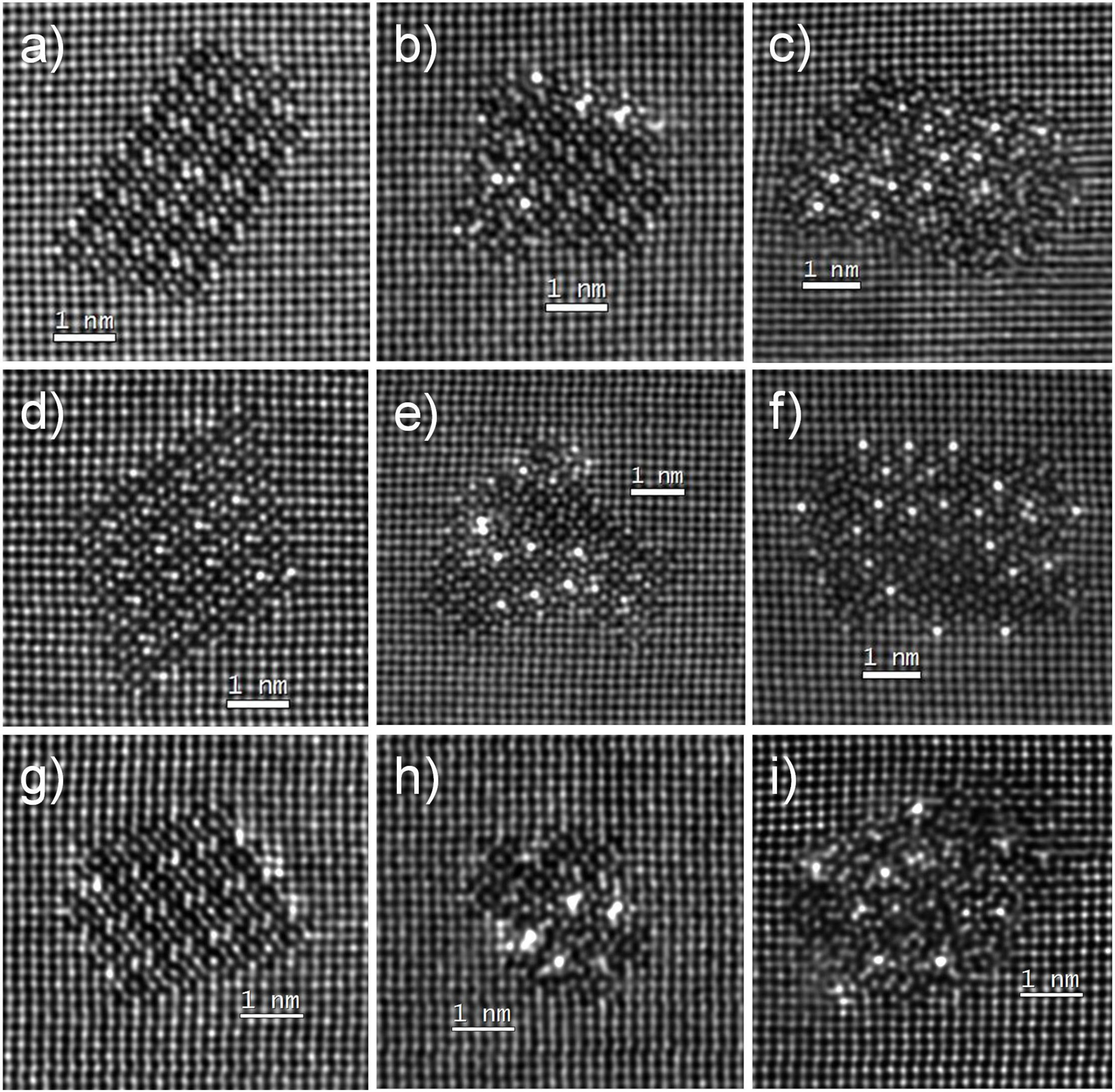
a)
1 nm
b)
1 nm
c)
1 nm
d)
1 nm
e)
1 nm
f)
1 nm
g)
1 nm
h)
1 nm
i)
1 nm

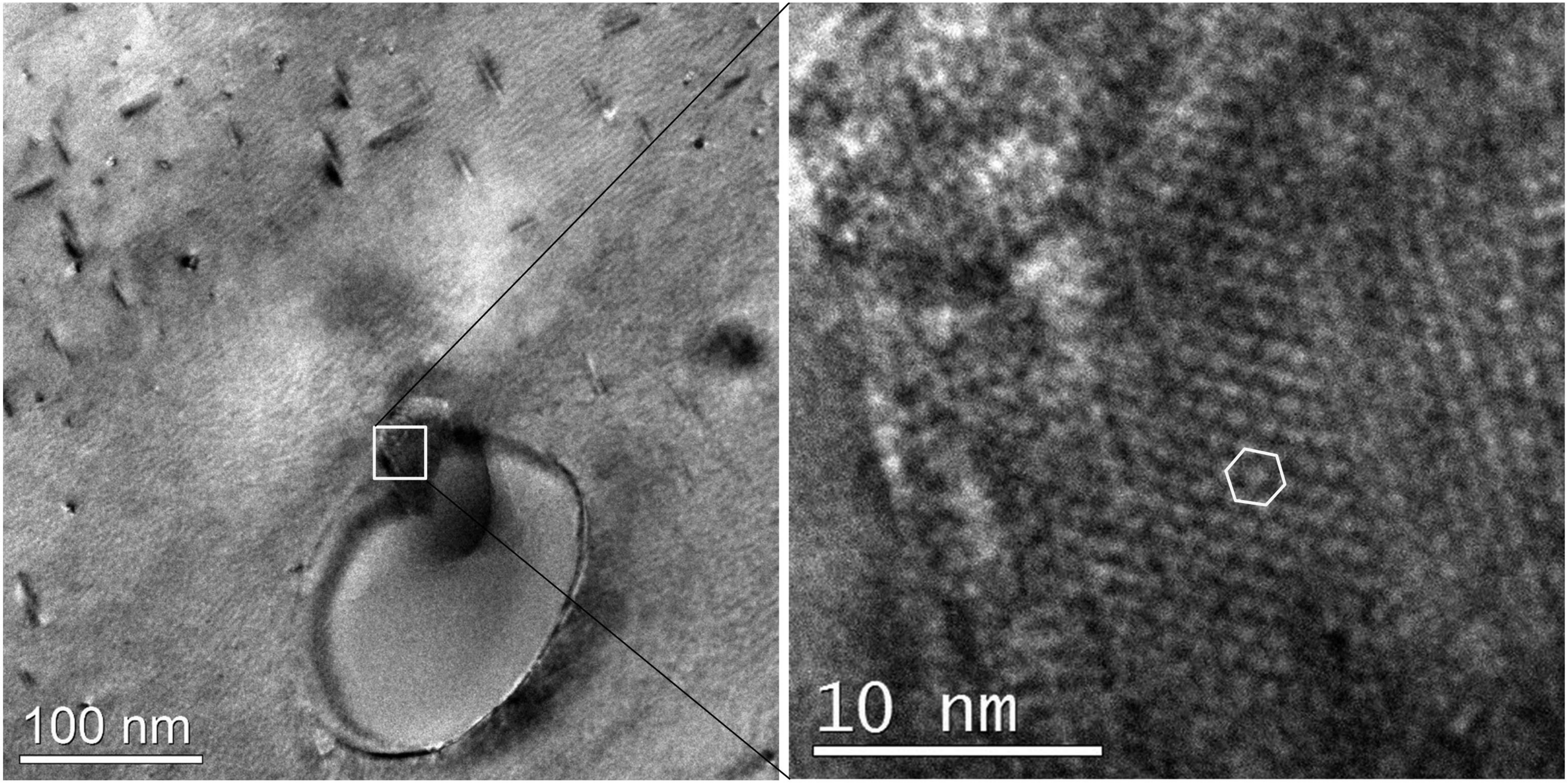
100 nm
10 nm

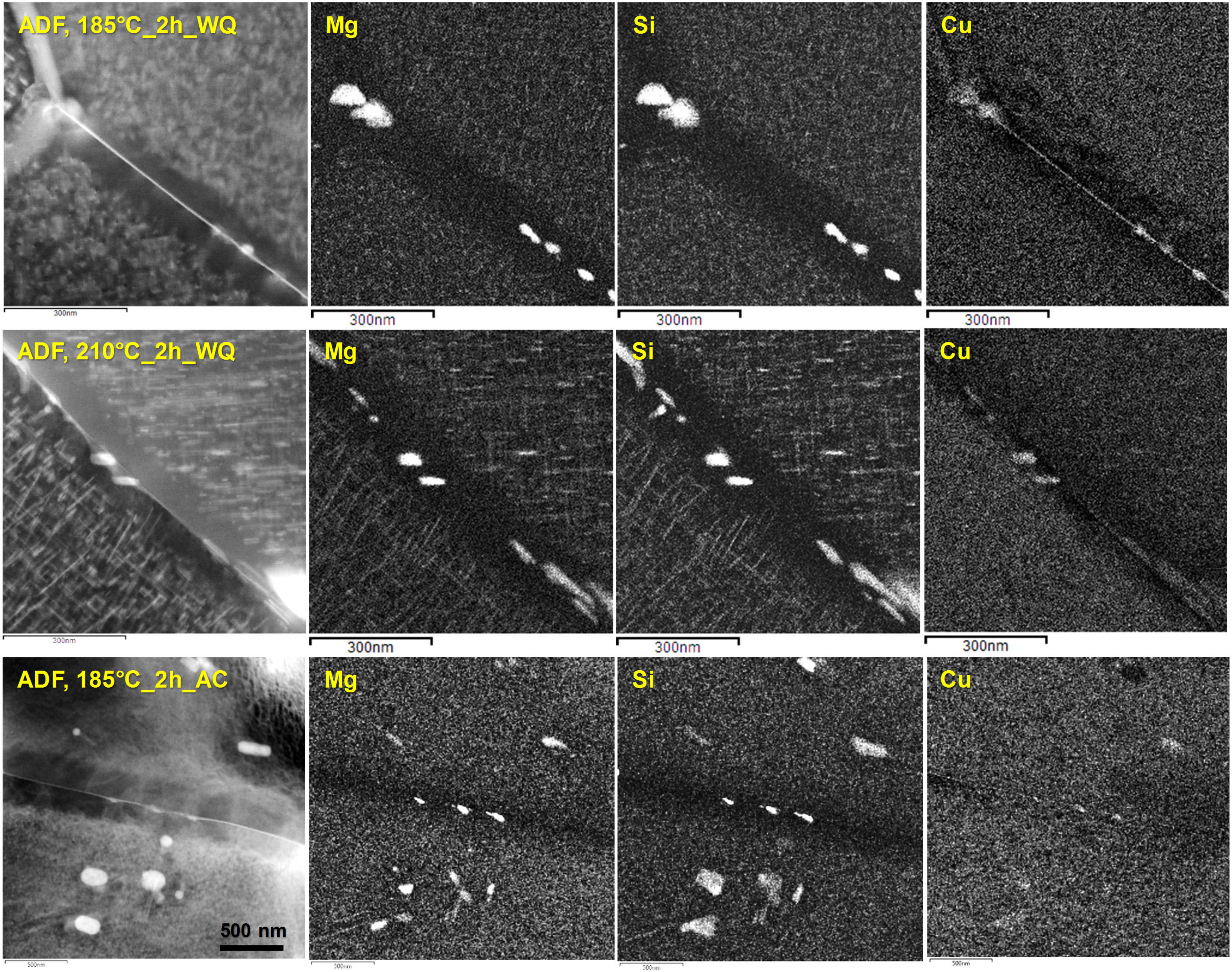

ADF, 185°C_2h_WQ
Mg
Si
Cu
300nm
300nm
300nm
300nm
ADF, 210°C_2h_WQ
Mg
Si
Cu
300nm
300nm
300nm
300nm
ADF, 185°C_2h_AC
Mg
Si
Cu
500 nm

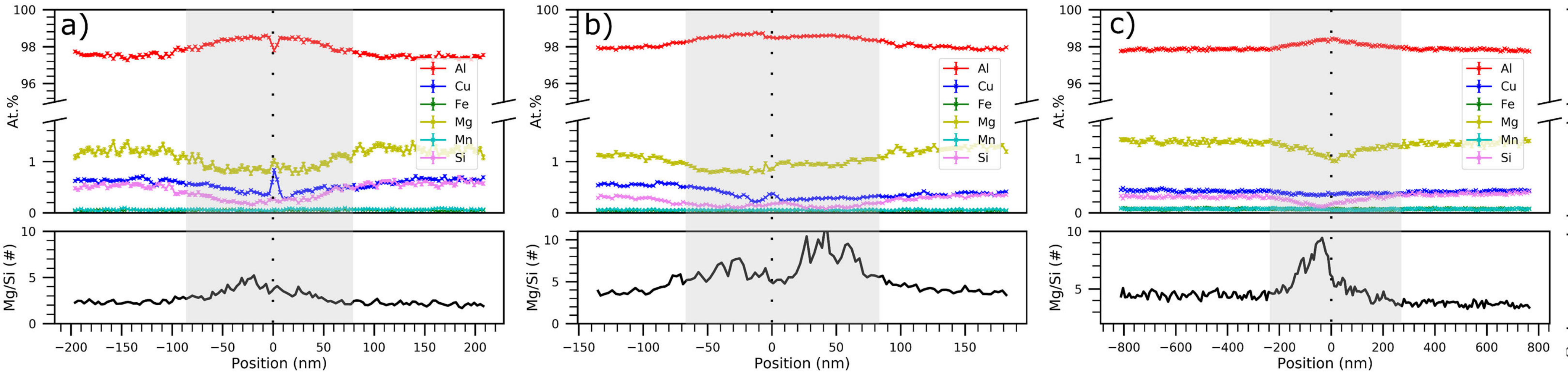
a)
b)
c)
Al
Cu
Fe
Mg
Mn
Si
At.%
Mg/Si (#)
Position (nm)

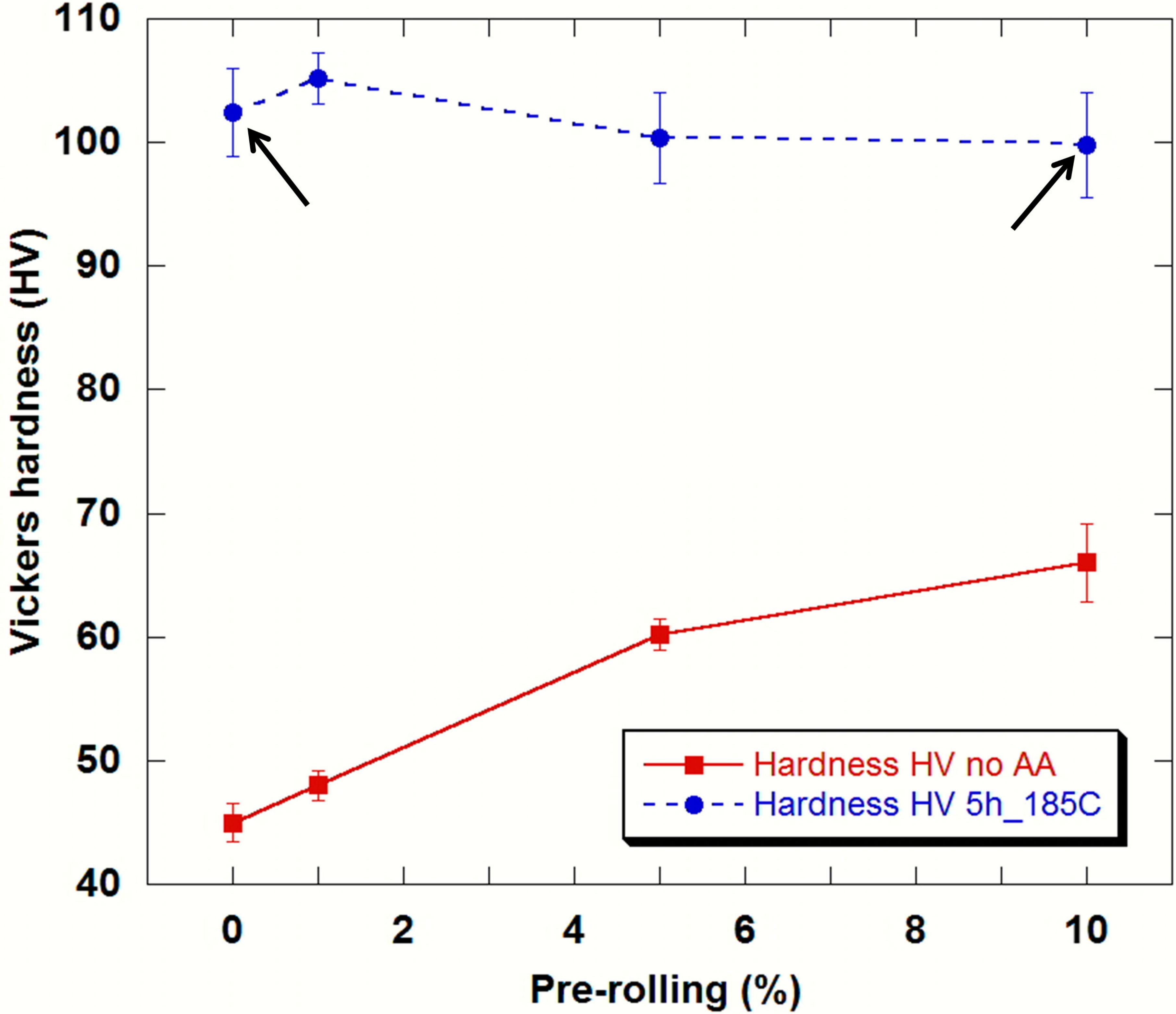

110
100
90
80
70
60
50
40
Vickers hardness (HV)
0
2
4
6
8
10
Pre-rolling (%)
Hardness HV no AA
Hardness HV 5h_185C

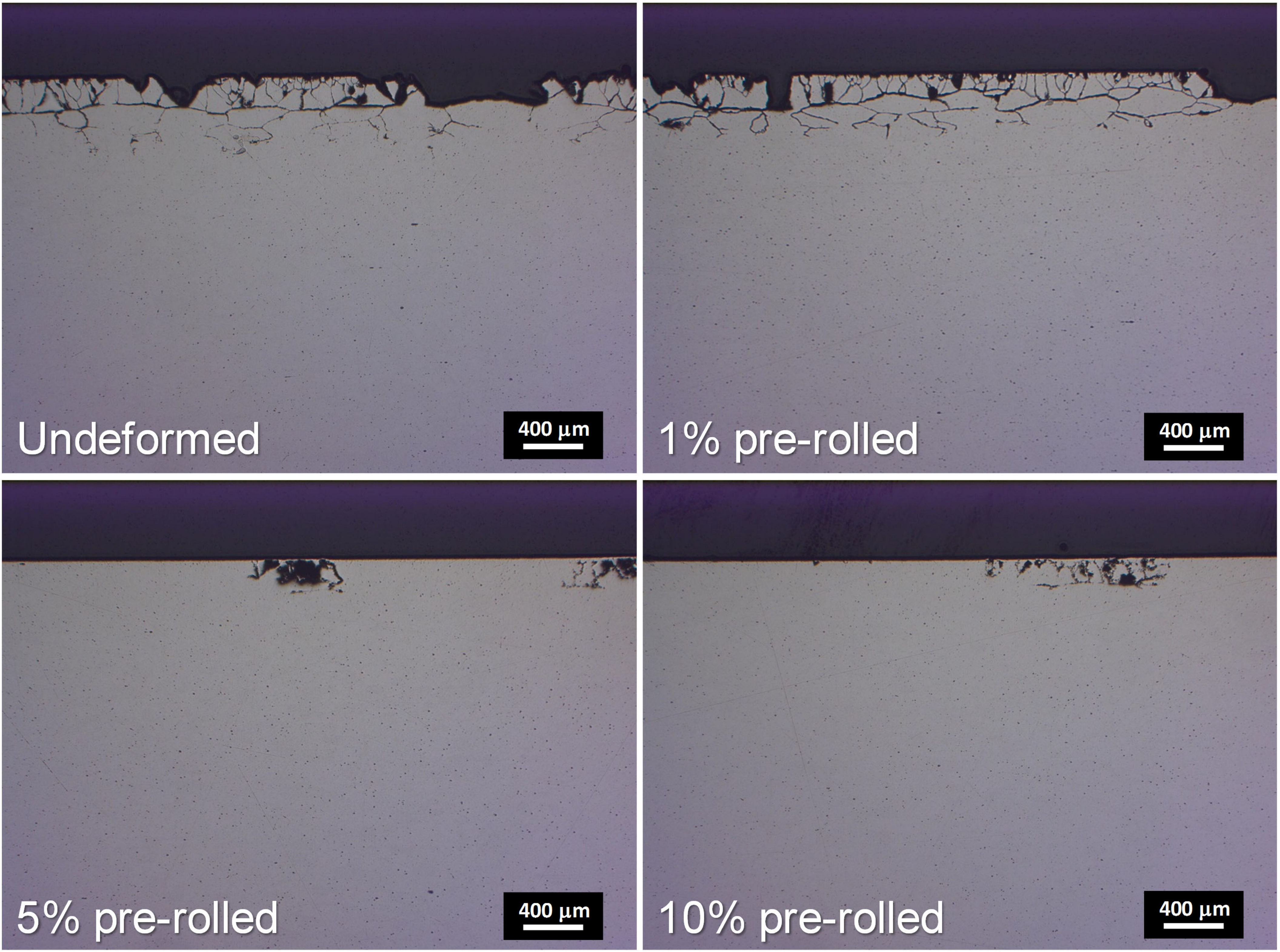
Undeformed
400 µm
1% pre-rolled
400 µm
5% pre-rolled
400 µm
10% pre-rolled
400 µm

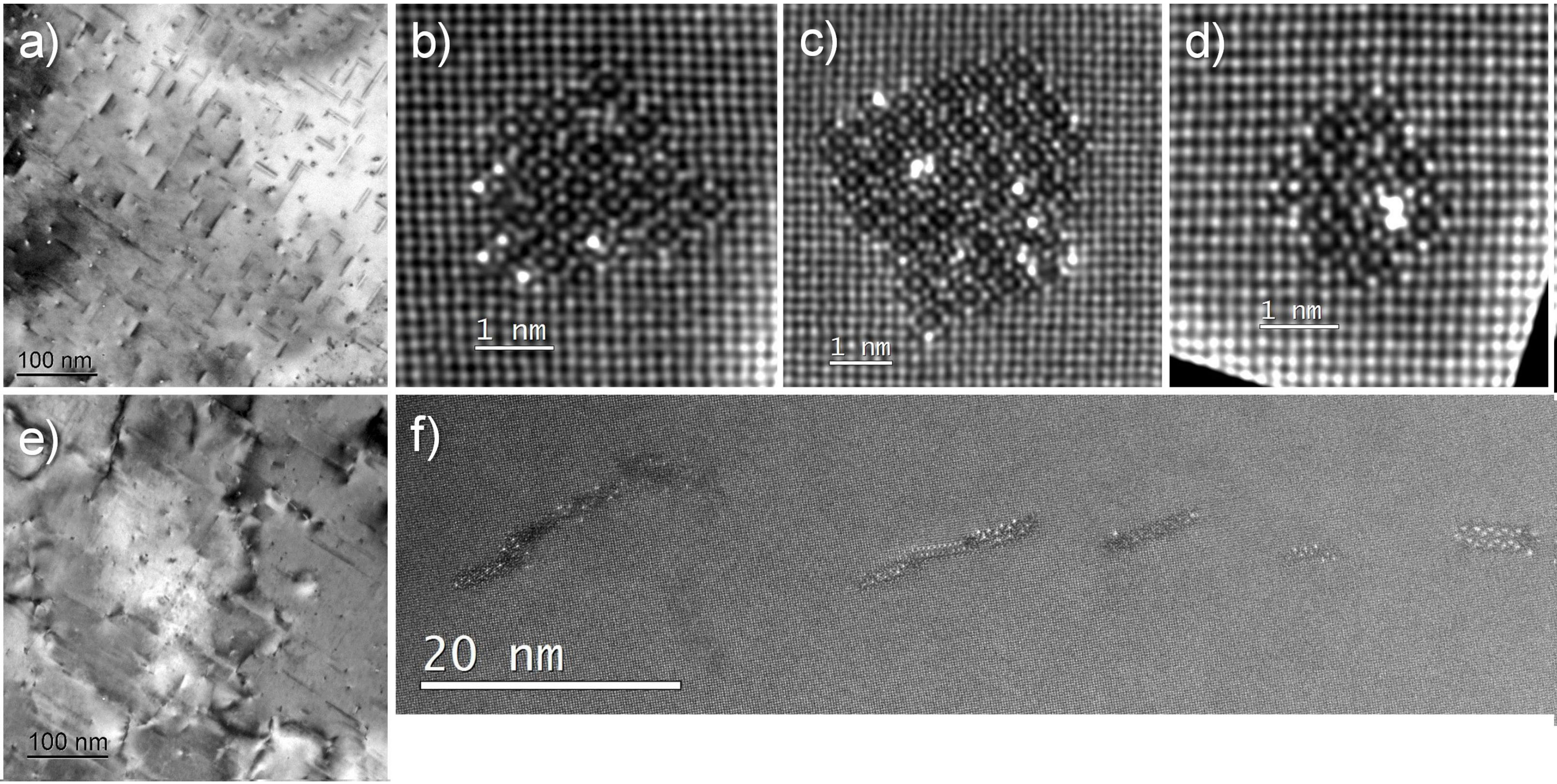
a)
100 nm
b)
1 nm
c)
1 nm
d)
1 nm
e)
100 nm
f)
20 nm

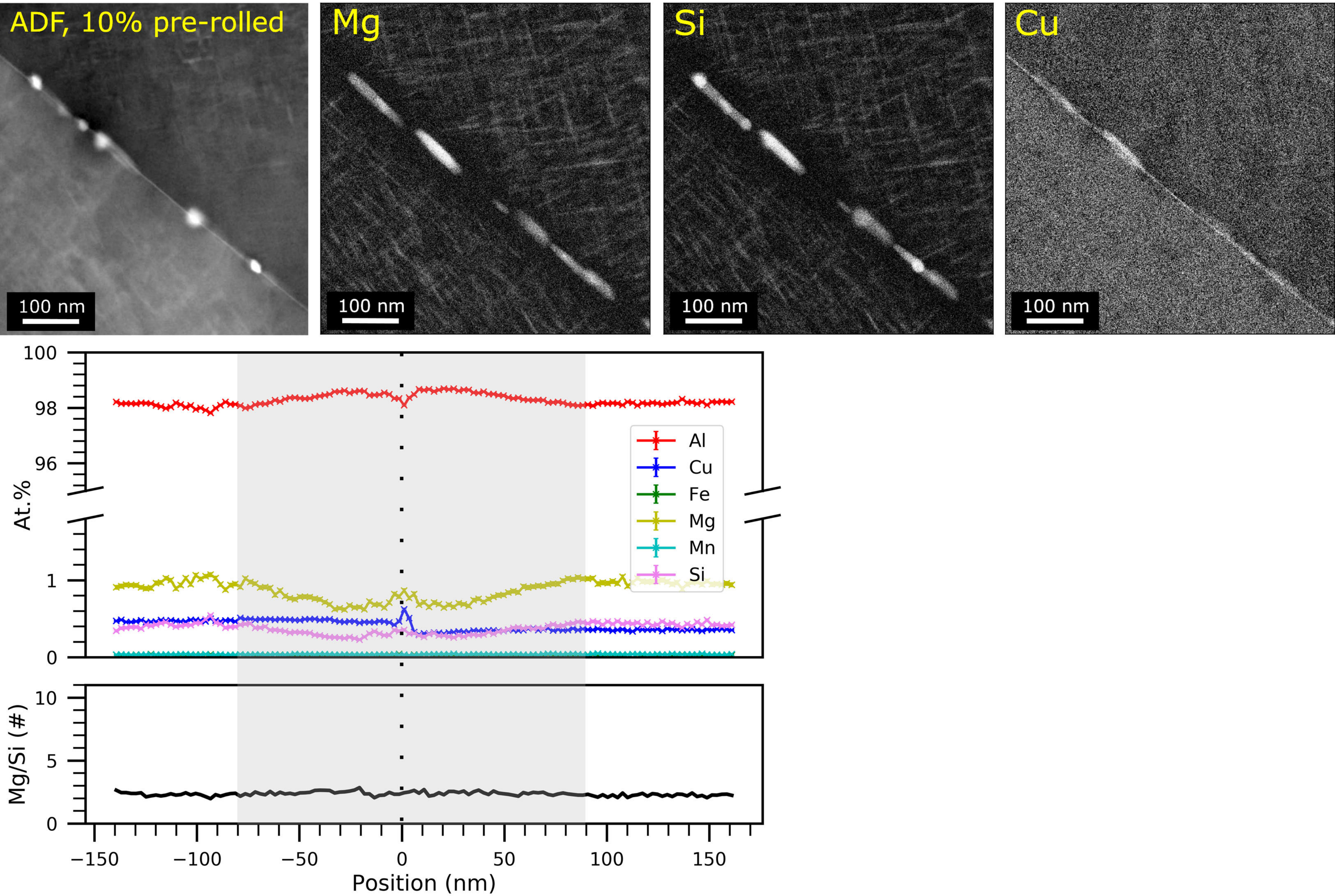
ADF, 10% pre-rolled
Mg
Si
Cu
100 nm
100 nm
100 nm
100 nm
At.%
100
98
96
1
0
Al
Cu
Fe
Mg
Mn
Si
Mg/Si (#)
10
5
0
−150
−100
−50
0
50
100
150
Position (nm)